Exploring highly deformed ground states involving the second intruder orbit in $Z > 50$ even-even nuclei

Tsunenori Inakura[1,*] Wataru Horiuchi[2,3,4,†] Shin'ichiro Michimasa,[4] and Masaomi Tanaka[5]

[1]*Office of Institute Strategy, Institute of Science Tokyo, Tokyo 152-8550, Japan*
[2]*Department of Physics, Osaka Metropolitan University, Osaka 558-8585, Japan*
[3]*Nambu Yoichiro Institute of Theoretical and Experimental Physics (NITEP), Osaka Metropolitan University, Osaka 558-8585, Japan*
[4]*RIKEN Nishina Center, Wako 351-0198, Japan*
[5]*Faculty of Arts and Science, Kyushu University, Fukuoka 819-0395, Japan*

(Received 6 February 2025; revised 28 September 2025; accepted 20 October 2025; published 3 December 2025)

We present a systematic survey of even-even nuclei with $Z > 50$ to identify where a very large prolate configuration driven by the second intruder orbit emerges. Within the energy density functional theory framework, we find in representative cases a pronounced prolate minimum at quadrupole deformation $\beta_2 \approx 0.3$–0.4. A characteristic feature of these minima is a local enhancement of the hexadecapole (β_4) component relative to nearby deformations, which is a clear fingerprint of the β_2-β_4 coupling expected for the second intruder orbit. Representative comparisons among three Skyrme interactions show a similar appearance of the highly deformed minimum and a local enhancement of β_4 at the prolate minimum, indicating qualitative robustness with respect to the interaction. The resulting maps highlight specific heavy nuclei where highly deformed ground states are anticipated.

DOI: 10.1103/7dpg-xh32

I. INTRODUCTION

Nuclear shapes and their evolution across the chart provide key information on shell structure away from stability and govern bulk observables such as charge radii, moments, total reaction cross sections, and fission barriers. Mapping where large deformations emerge—and which multipole components accompany them—provides benchmarks of energy density functional (EDF) descriptions.

In a recent analysis of the neutron-rich zirconium isotope ^{112}Zr ($Z = 40$, $N = 72$) [1], we demonstrated within a self-consistent EDF framework that the onset of partial occupancy of the second intruder orbit can stabilize a very large prolate shape. Under standard EDF conditions, the potential energy surface develops a pronounced minimum around quadrupole deformation $\beta_2 \approx 0.4$. These results motivate a systematic assessment of how generic this intruder-driven mechanism is, and how robust it remains with respect to the effective interaction in heavier even-even systems.

Quadrupole-hexadecapole (β_2-β_4) shapes affect bulk observables such as charge radii and total reaction cross sections, and can also influence the outer part of fission paths. It is well established that the β_2-β_4 coupling is strong; pure β_4 minima are exceptional, while sizable β_4 components typically accompany large quadrupole deformation [2,3]. Recent beyond-mean-field studies report that these (β_2, β_4) trends are robust under reasonable interaction changes, and surveys in heavy systems likewise stress the role of higher multipoles along fission trajectories [3–6].

Guided by the ^{112}Zr case, we survey even-even nuclei with $Z > 50$ with the aim of exploring where the second intruder mechanism actually materializes. In representative nuclei within this region the calculated deformation landscapes exhibit a pronounced prolate minimum at $\beta_2 \approx 0.3$–0.4. A characteristic feature at the minimum is an enhanced hexadecapole component relative to its surroundings, providing a clear manifestation of the β_2-β_4 coupling. The present maps indicate where highly deformed ground states are expected in heavy systems and what β_4 response they carry, while keeping the scope intentionally simple (axial symmetry, a common HO basis truncation, no triaxial or octupole degrees of freedom).

The paper is organized as follows. Section II summarizes the common setup used in all calculations. Section III presents the systematics and the interaction dependence, including an overlay figure that illustrates the robustness of the large prolate minimum across SkM*, SLy4, and UNEDF1. Section IV concludes with the main findings, scope, and limitations.

II. METHOD

We perform a systematic calculation of ground-state properties of even-even nuclei from Te ($Z = 52$) to Hg ($Z = 80$) isotopes by the Skyrme Hartree-Fock-Bogoliubov (HFB) model using the HFB solver, HFBTHO [7]. Deformation energy curves are obtained with an axial HFB calculation. The quadrupole moment Q_{20} (i.e., β_2) is constrained by a standard quadratic term, and at each fixed β_2 the HFB energy is minimized. Other multipoles are not constrained in this work. The

*Contact author: inakura@gmail.com
†Contact author: whoriuchi@omu.ac.jp

single-particle wave functions are expanded in an axially deformed harmonic-oscillator basis including all major shells up to $N_{\max} = 14$. We find this size adequate to describe the global systematics discussed below. For some selected heavy nuclei we also increased the basis and saw only modest changes in bulk observables. The same truncation is used for all nuclei. At each constrained value of β_2, we adjust the aspect ratio of the axially deformed HO basis to approximately follow the target deformation, in order to reduce basis-shape mismatch. No nucleus-specific tuning is applied. The SkM* interaction is employed [8] as it is known to reasonably describe nuclear deformations. The SLy4 [9] and UNEDF1 [10] interactions have been used to check the dependence of the results on the interaction considered in the calculations. A standard mixed-type pairing interaction [11] is used. In this work, we use only axial HFB solutions. We focus on global trends such as the rms radii, diffuseness, and reaction cross sections, which are dominated by the bulk deformation and density profile. In many even-even nuclei, the change in the rms radius when triaxiality is allowed is usually modest compared with spectroscopic effects. Large-scale EDF studies that include triaxial shapes reproduce charge-radius systematics well and support this view [2,12]. At the same time, there are known γ-soft regions (e.g., Os-Pt) where triaxiality can be relevant, and recent studies in Ru isotopes also indicate that triaxiality may affect radius [13]. Therefore, our axial results should be seen as a simple trend map.

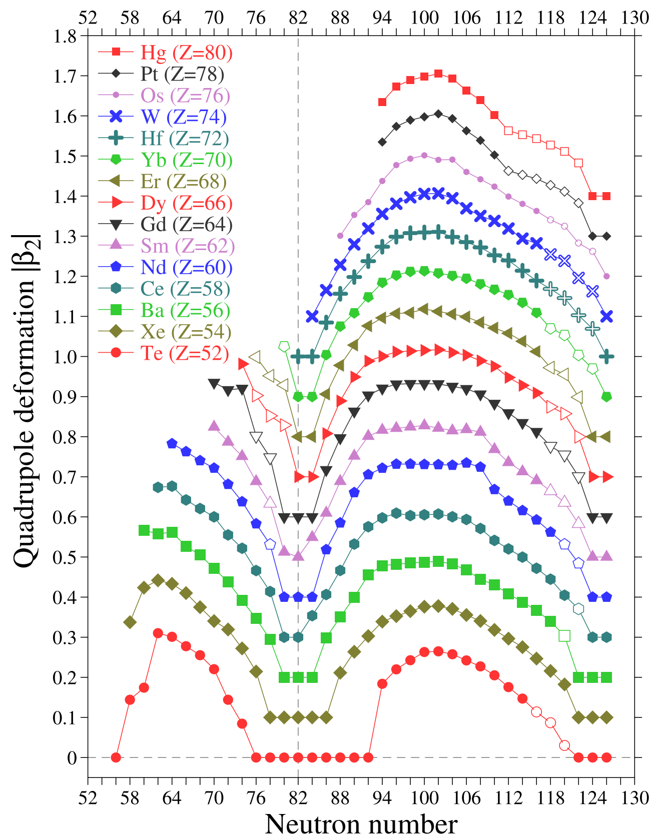

FIG. 1. Quadrupole deformation parameters $|\beta_2|$ of even-even nuclei from the proton dripline to $N = 126$ of Te ($Z = 52$) to Hg ($Z = 80$) isotopes as a function of the neutron number. For visibility, the $|\beta_2|$ value of each isotope is shifted by $0.05 \times (Z - 52)$ and oblate shapes ($\beta_2 < 0$) are represented by open symbols.

III. NUMERICAL RESULTS

A. Exploring the characteristic deformation in $Z > 50$ even-even nuclei

1. Heavy mass region

Figure 1 displays the quadrupole deformation parameters $|\beta_2|$ of even-even nuclei from Te ($Z = 52$) to Hg ($Z = 80$) isotopes as a function of the neutron number from the proton dripline to $N = 126$. Open symbols denote oblate deformation ($\beta_2 < 0$). All isotopes are spherical at $N = 82$ and show gradual enhancement of the β_2 values for $N > 82$. The deformation grows with increasing N by the neutron occupation of the intruder [550]1/2 orbit coming from the spherical $0h_{11/2}$ orbit, and the β_2 values reach up to ≈ 0.3 at $N \approx 100$. For $N \gtrsim 100$, the deformations of the ground states become smaller, and change to oblate shapes. At $N \approx 126$, the ground states become spherical again. While all isotopes have similar behaviors of the deformation of the ground states, only Nd ($Z = 60$) and Sm ($Z = 62$) isotopes exhibit kinks of the β_2 values at $N = 106$ and 108. The proton number 60 may have some relations with the onset of the large deformation in ^{100}Zr with the neutron number 60 [14].

The hexadecapole deformation β_4 serves an indicator of the occupation of the second intruder orbit as it is enhanced by the occupation of an elongated orbit [1,15]. Figure 2 displays the calculated β_4 values of the isotopes. The β_4 values, linking to β_2, increase gradually for $N > 82$ due to the fractional neutron occupation of the intruder [550]1/2 orbit, reaching maximum values at $N \approx 90$. Following this peak, the β_4 values decrease gradually and become negative values, approaching to zero at $N \approx 126$. In several isotopes, the hexadecapole deformations jump at $N \approx 120$, which corresponds to the shape changes from prolate to oblate deformations shown in Fig. 1. Similar to β_2, there are bumps of β_4 in Nd and Sm isotopes at $N = 106$ and 108. Therefore, ^{166,168}Nd and ^{168,170}Sm likely have the ground states involving the second intruder orbit.

We plot in Fig. 3 the proton and neutron single-particle energies of ^{166}Nd as a function of the quadrupole deformation parameter β_2. The deformation energy, which is measured from the parameter with the spherical shape ($\beta_2 = 0$), is also plotted as a guide. We see that the deformation energy of ^{166}Nd has the minimum at $\beta_2 = 0.33$, showing large quadrupole deformation. In ^{166}Nd, the asymptotic quantum number of the most elongated orbit is [660]1/2, which comes from the spherical $0i_{13/2}$ orbit. Since the nuclear deformation is so large, the elongated, next intruder orbit with [651]1/2 coming from the spherical $1g_{9/2}$ orbit is occupied with an occupation probability 0.48. The hexadecapole deformation parameter is also large, $\beta_4 = 0.11$. This second intruder orbit plays a role in forming the shell gaps at $N = 106$, and hence such a large deformation is stabilized. Note that proton single-particle energies also have a large shell gap with

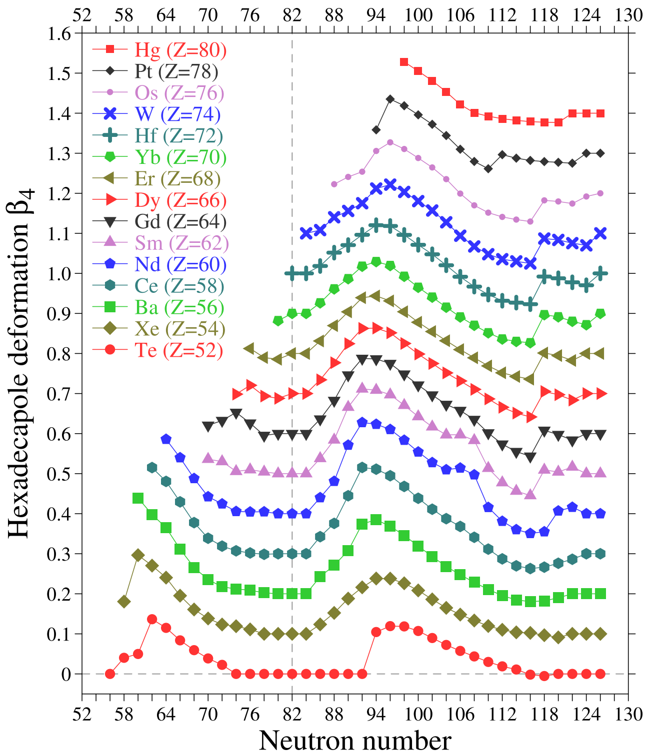

FIG. 2. Hexadecapole deformation parameters β_4 of even-even nuclei from the proton dripline to $N = 126$ of Te ($Z = 52$) to Hg ($Z = 80$) isotopes as a function of the neutron number. For visibility, the β_4 value of each isotope is shifted by $0.05 \times (Z - 52)$.

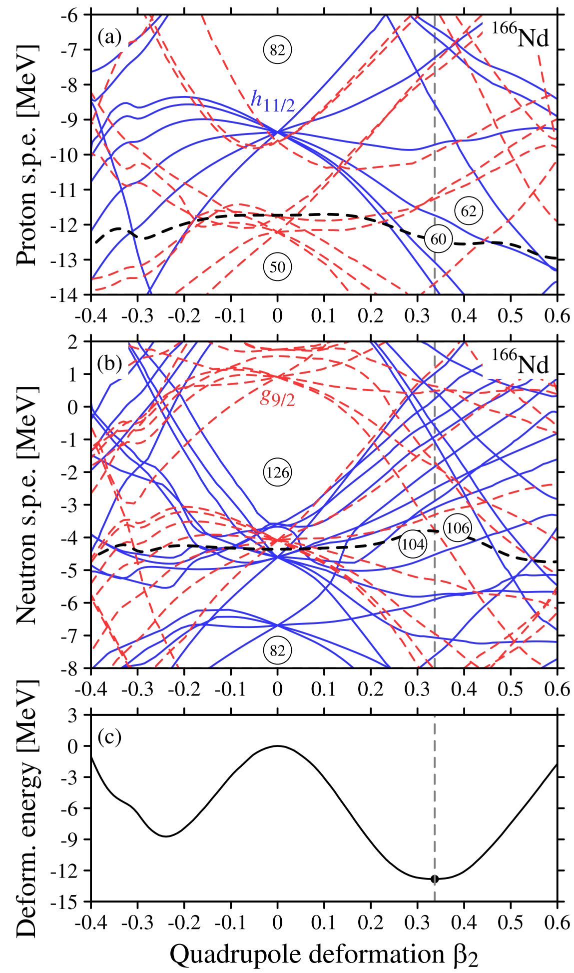

FIG. 3. (a) Proton and (b) neutron single-particle energies (s.p.e.) and (c) deformation energies of ^{166}Nd as a function of quadrupole deformation parameter β_2. Blue solid and red dashed curves in panels (a) and (b) present negative and positive parity single-particle levels, respectively. Thick dashed curves denote the proton and neutron chemical potentials. A vertical dotted line indicates the β_2 value of the ground state for a guide to the eye.

$Z = 60$ at large deformation, occupying the enlarged orbits with [550]1/2 and [541]3/2. Both neutrons and protons favor the large deformation.

Recent beyond-mean-field studies show that β_2 and β_4 are strongly linked. In the rare-earth region (Sm and Gd), a Gogny HFB plus generator coordinate method (GCM) calculation finds that including β_4 dynamics gives extra correlation energy of a few hundred keV, and produces low-lying 0^+ states with mixed (β_2, β_4) character [3]. For heavy nuclei (Ra-Pu), a microscopic study reports a similar coupling pattern, a small but stable negative β_4 region near $N \approx 184$ even after zero-point motion, and a change of the coupling strength along the isotopic chains [4]. These works also show that the minimum can shift when β_4 is included. Our mean-field maps are consistent with these general trends. Here we provide a broad systematics and the link to second intruder occupation while a full GCM analysis is outside the scope of the present survey.

At the prolate β_2 minimum, the "depth" along β_4 can be quantified by the curvature of the collective potential with respect to β_4, i.e. the second derivative $\partial^2 E/\partial \beta_4^2$. The coupling between β_2 and β_4 is captured by the cross second derivative $\partial^2 E/\partial \beta_2 \partial \beta_4$. Earlier beyond-mean-field analyses [3,4] show that such β_2-β_4 coupling can be sizable and may shift minima by up to the MeV scale in selected isotopic chains. In this paper, β_4 is used mainly as a global indicator and we focus on systematic trends. A dedicated two-dimensional (β_2, β_4) study for a few benchmark nuclei, including explicit evaluations of these curvatures, will be pursued next.

2. Proton-rich region

We also find a contribution of the second intruder orbit in a proton-rich nucleus ^{138}Gd with $Z = 64$ and $N = 74$ as indicated by the kink behavior seen in Figs. 1 and 2. The deformation energy and proton and neutron single-particle levels of ^{138}Gd are shown in Fig. 4. Calculated ^{138}Gd is highly deformed, with the energy minimum at $\beta_2 = 0.33$ and $\beta_4 = 0.05$. In the ground state of ^{138}Gd, the second intruder neutron orbit originating from the spherical $1f_{7/2}$ orbit is occupied with an occupation probability 0.73, following the same mechanism in neutron-rich nuclei ^{112,114}Zr [1]. Additionally, the proton shell structure shows a gap with $Z = 64$ at large β_2. We remark that the ground state of ^{138}Gd is observed, showing a large quadrupole deformation [16].

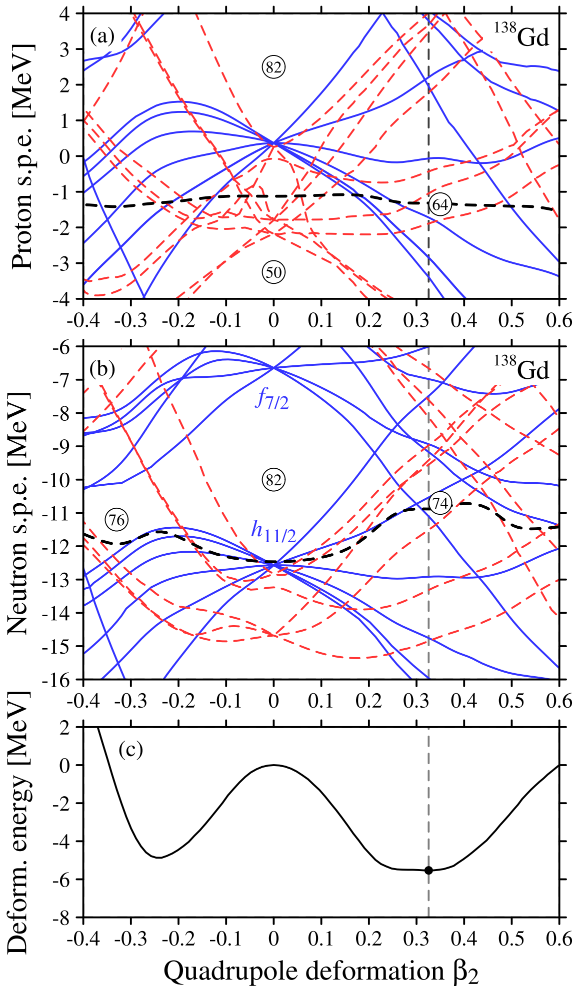

FIG. 4. Same as Fig. 3 but for ^{138}Gd.

3. *Case of ^{272}No*

The deformation energy curve for ^{272}No is obtained from axial HFB calculations using an axially deformed HO basis truncated at $N_{\max} = 14$, as shown in Fig. 5. For such a heavy neutron-rich nucleus, the depths of the minima can change when we use a larger basis. We tried a larger basis and saw only modest changes in bulk values (energy differences along

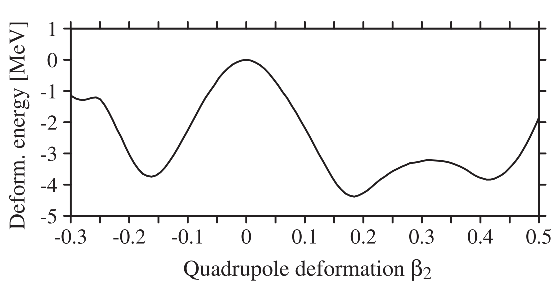

FIG. 5. Deformation energy curve for ^{272}No obtained from axial HFB calculations with the HFBTHO solver, using an axially deformed harmonic-oscillator basis truncated at $N_{\max} = 14$. Octupole deformation (β_3) is not included.

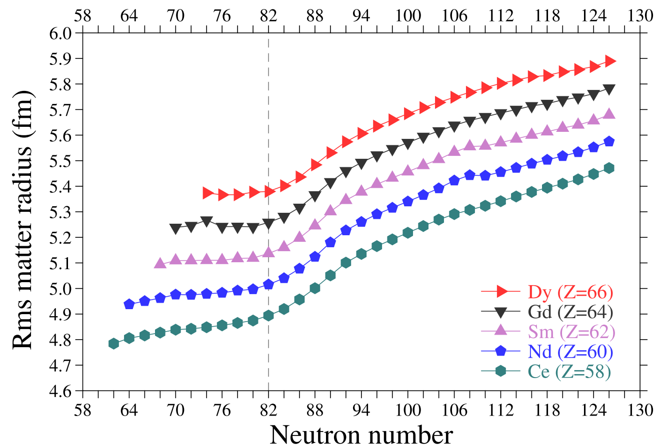

FIG. 6. Matter radii of Ce, Nd, Sm, Gd, and Dy isotopes as a function of neutron number. For visibility, the values are shifted by $0.05 \times (Z - 58)$ fm.

the curve, β_2, β_4, rms radius), so the global picture stays the same. We still find a prolate minimum near $\beta_2 \approx 0.4$ connected to the second intruder. This minimum looks robust, but we cannot decide if it is the ground state or an excited one within the present model; adding β_3 and a larger basis could change the ordering. Octupole shapes (β_3) are important in actinides and superheavy nuclei and often lower the third barrier and modify a shallow third minimum [5,6].

B. Observables

Here we discuss possible observables to identify this characteristic deformation.

The occupation of the second intruder orbit is reflected in the density profiles near the nuclear surface. Figure 6 plots the matter radii of these isotopes. We see kink behavior at $N \approx 106$ for Nd and Sm isotopes although the changes seem to be small.

This difference becomes more apparent by analyzing the diffuseness of the matter density distribution $\rho(r)$ at the surface region [17]. Assuming the model density distribution of the two-parameter Fermi (2pF) function, $\rho_{\rm 2pF}(r) = \rho_0\{1 + \exp[(r - R)/a]\}$. The radius R and diffuseness parameters a are obtained by minimizing [17]: $\int_0^\infty dr\, r^2 |\rho(r) - \rho_{\rm 2pF}(r)|$. Figure 7 draws the diffuseness parameter extracted from the matter density distribution obtained by the present HFB calculations. Apparently, the nuclear surface becomes more diffused and produces the kink behavior in the a values when the elongated second intruder orbit is occupied at $N = 70$ and 106. As shown in Ref. [17], the diffuseness can be determined by measuring the medium- to high-energy proton-elastic scattering cross sections at the first peak position. It is desirable to systematically measure these cross sections to detect the structure change, which is very unique in an isotopic chain of the highly deformed states.

Another possibility is to measure the total reaction or interaction cross sections at medium to high incident energies. The total reaction and elastic scattering cross sections are useful to study the size properties of unstable nuclei [18].

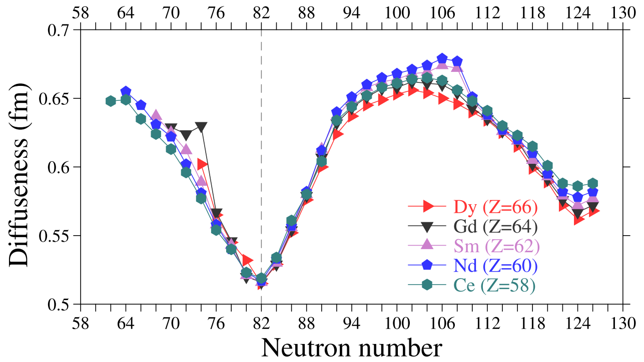

FIG. 7. Diffuseness parameters of Ce, Nd, Sm, Gd, and Dy isotopes extracted from these matter density distributions as a function of neutron number.

The cross section calculations are well established and can be obtained by using a high-energy reaction theory, the Glauber theory [19]. We use the same setup to calculate the total reaction cross section as Refs. [1,15]. The inputs to the theory are the nuclear density distributions and the profile function which reproduces the nucleon-nucleon scattering properties. A standard parameter set of the profile function is used and is tabulated in Ref. [20]. For a carbon target, we employ a harmonic-oscillator type density distribution reproducing the experimental charge radius. It should be noted that no *ad hoc* parameter is introduced after all the inputs are set. The validity of this approach has been confirmed in many examples of medium- to high-energy nuclear reactions involving unstable nuclei [21–25].

It is known that the size properties of the nuclear ground state are well reflected in the total reaction cross section at a few to several hundred MeV/nucleon. To discuss the feasibility of detecting the kink due to the occupation of the second intruder orbit, we compute the total reaction cross sections using the density distributions obtained by the HFB model. Note that the density distribution in the HFBTHO code is the intrinsic one and is converted to the laboratory frame density $\rho(r)$ by averaging the intrinsic density distribution over angles as prescribed in Ref. [21]. Figure 8 plots the calculated total reaction cross sections on proton and carbon targets. Incident energy is chosen at 300 MeV/nucleon as it is a typical incident energy at RIKEN [26]. For a proton target, the cross section behavior is similar to that of the matter radii, while for a carbon target, the kink behaviors around $N = 70$ and 106 are more pronounced. The above observations can be understood by recalling that the cross section on a proton target well reflects the change of the nuclear radii but is less sensitive to the surface part of the nuclear density distribution than that on a carbon target [27]. In the sense of the sensitivity to the nuclear surface, a nuclear target is in general more advantageous than the proton target to probe the kink behavior due to the occupation of the second intruder orbit.

C. Interaction dependence

We repeated the calculations with three Skyrme interactions (SkM*, SLy4, UNEDF1) using the same setup. Figure 9 shows a representative case (^{166}Nd) in the second intruder region. SkM*, SLy4, and UNEDF1 produce a common large prolate minimum at $\beta_2 \approx 0.35$. The curves almost overlap, indicating only modest differences in depth and local stiffness. We also note a small change of curvature around $\beta_2 \approx 0.30$, consistent with the onset of the second intruder configuration. Together, these features demonstrate that the appearance of the highly deformed ground state is robust against the

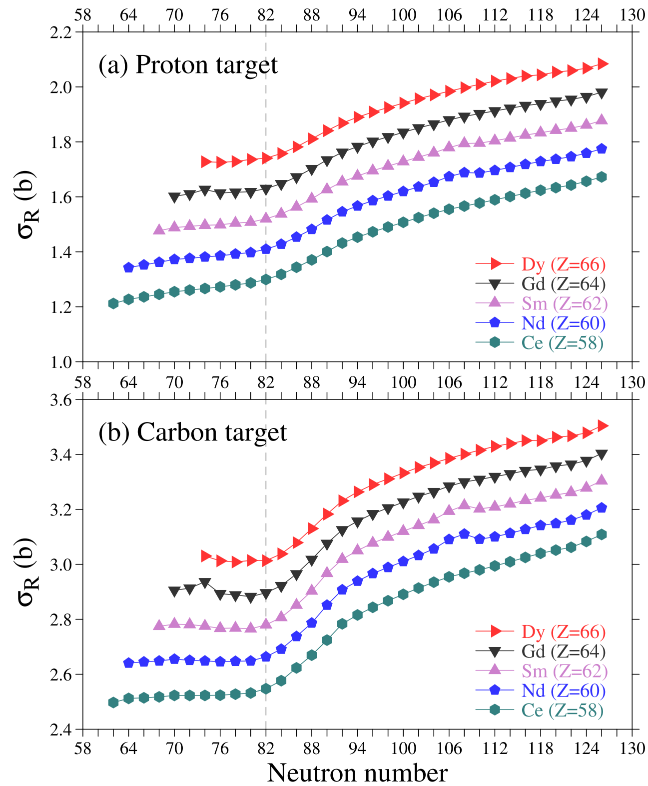

FIG. 8. Total reaction cross sections of Ce, Nd, Sm, Gd, and Dy isotopes on (a) proton and (b) carbon targets at 300 MeV/nucleon as a function of neutron number. For visibility, the cross sections are shifted by $0.05 \times (Z - 58)$.

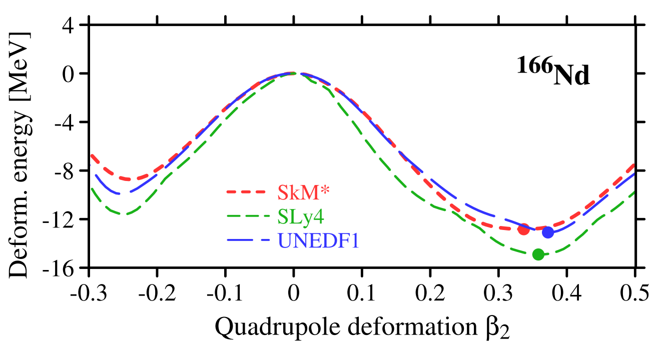

FIG. 9. Axial-HFB (HFBTHO) deformation-energy curve of ^{166}Nd. Energies are shifted to the spherical point (β_2=0). SkM*, SLy4, and UNEDF1 give the same large prolate minimum at $\beta_2 \approx 0.35$; differences are small. A curvature change around $\beta_2 \approx 0.3$ indicates the emergence of the second intruder minimum.

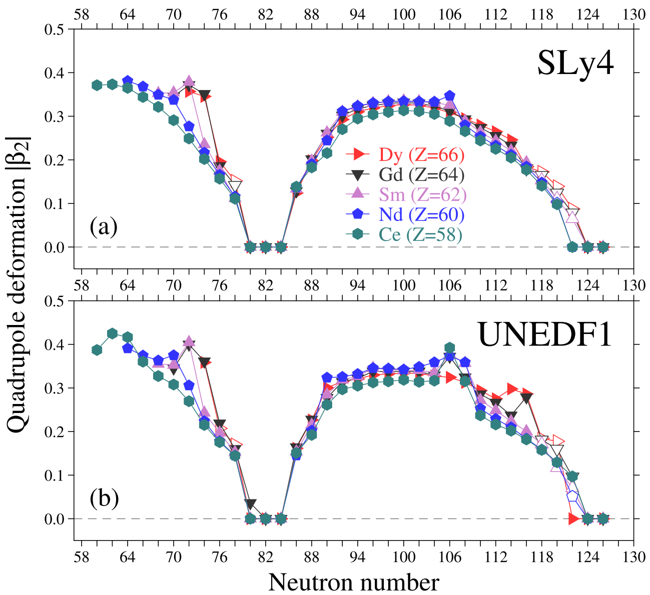

FIG. 10. Quadrupole deformation parameters $|\beta_2|$ of even-even nuclei from the proton dripline to $N = 126$ in Ce, Nd, Sm, Gd, and Dy isotopes as a function of neutron number calculated with (a) SLy4 and (b) UNEDF1 interactions. For visibility, oblate shapes ($\beta_2 < 0$) are represented by open symbols.

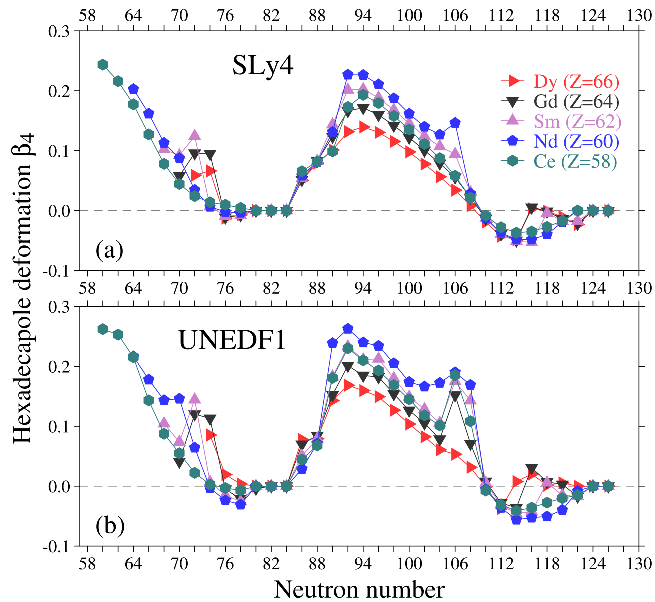

FIG. 11. Hexadecapole deformation parameters β_4 of even-even nuclei from the proton dripline to $N = 126$ in Ce, Nd, Sm, Gd, and Dy isotopes as a function of neutron number calculated with (a) SLy4 and (b) UNEDF1 interactions.

choice of Skyrme interaction. At the prolate minimum, the extracted β_4 is similar among the three interactions, and the three curves overlap closely in a small window around the minimum, suggesting a qualitatively robust β_2-β_4 coupling (see Sec. III A). This interaction-robust behavior agrees with a Gogny HFB + GCM analysis in the rare-earth region, which found stable (β_2, β_4) trends under reasonable interaction changes [3].

As we discussed in Sec. III A, the appearance of the ground state involving the second intruder orbit strongly depends on the shell structure. Here we investigate the interaction dependence of the present findings. Figures 10 and 11, respectively, display the quadrupole and hexadecapole deformation parameters of even-even nuclei of Ce ($Z = 58$) to Dy ($Z = 66$) isotopes, calculated with SLy4 [9] and UNEDF1 [10] interactions. The SLy4 results predict the occupation of the second intruder orbit in ^{166}Nd and ^{168}Sm at $N \approx 106$ where the sudden enhancement of the values of β_2 and β_4 is obtained, as in the SkM* case. The UNEDF1 results predict the occupation in ^{164}Ce, ^{166,168}Nd, ^{168,170}Sm, and ^{170}Gd. For nuclei with $Z \approx 64$ and $N \approx 116$, UNEDF1 produces highly deformed ground states involving the occupation of the second intruder [651]1/2 orbit from the spherical $1g_{9/2}$ orbit, which is the same orbit to that in ^{166,168}Nd, as shown in Fig. 12. In the proton-rich region, both the SLy4 and UNEDF1 produce the occupation of the second intruder orbit in ^{134}Sm and ^{136,138}Gd, and proton-dripline nuclei of Dy isotopes. Therefore, all the Skyrme interactions employed produce enlarged-deformed ground states in ^{138}Gd, ^{166}Nd, and ^{168}Sm, indicating the robust occupation of the second intruder orbit in this region.

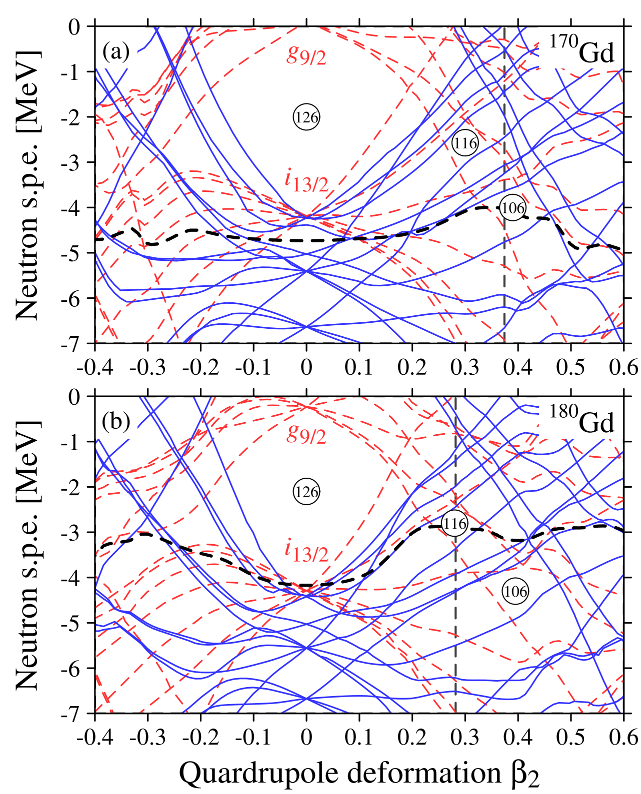

FIG. 12. Neutron single-particle energies (s.p.e.) of (a) ^{170}Gd and (b) ^{180}Gd as a function of quadrupole deformation parameter β_2, calculated with UNEDF1 interaction.

IV. SUMMARY

We performed a systematic axial HFB (HFBTHO) survey with a common setup and focused on the region where the second intruder drives a highly-deformed state.

A. Robust appearance of a highly deformed state

For representative nuclei in the second intruder region, all three Skyrme interactions (SkM*, SLy4, UNEDF1) produce a common large prolate minimum at $\beta_2 \approx 0.35$. An overlay figure shows that the curves almost overlap; the minimum appears in the same place with small quantitative differences. This means the appearance of the highly deformed state is robust against the interaction choice.

B. Hexadecapole trends and coupling

At the prolate minimum, the extracted β_4 values are similar among the three interactions, and the curve shapes near the minimum are comparable. This points to a qualitatively robust β_2-β_4 coupling associated with the second intruder configuration.

C. Systematics and scope

Along rare-earth chains (e.g., Nd-Sm-Gd), we find the same qualitative picture: a common highly deformed prolate minimum at $\beta_2 \approx 0.35$ across SkM*, SLy4, and UNEDF1. A superheavy example, ^{272}No, is shown separately as an illustrative case; we do not include it in the robustness because octupole and basis-size effects may change the ordering.

D. Limitations

We used axial HFB with a fixed HO basis truncation and did not include octupole (β_3) or triaxial shapes. For very heavy nuclei the energy ordering of competing minima may change when β_3 and a larger basis are included.

E. Outlook

The next step is a focused two-dimensional (β_2, β_4) analysis for a few benchmark nuclei and the explicit inclusion of octupoles (β_3) in heavy systems to fix the ordering when two minima compete within a few hundred keV. This will turn the present trend map into quantitative predictions.

ACKNOWLEDGMENTS

This work was in part supported by Japan Society for the Promotion of Science (JSPS) KAKENHI Grants No. 23K22485, No. 25K07285, and No. 25K01005 and JSPS Bilateral Program No. JPJSBP120247715.

DATA AVAILABILITY

The data that support the findings of this article are not publicly available. The data are available from the authors upon reasonable request.

[1] W. Horiuchi, T. Inakura, S. Michimasa, and M. Tanaka, Phys. Rev. C **107**, L041304 (2023).
[2] J.-P. Delaroche, M. Girod, J. Libert, H. Goutte, S. Hilaire, S. Péru, N. Pillet, and G. F. Bertsch, Phys. Rev. C **81**, 014303 (2010).
[3] C. V. Nithish Kumar and L. M. Robledo, Phys. Rev. C **108**, 034312 (2023).
[4] R. Rodríguez-Guzmán and L. M. Robledo, Phys. Rev. C **111**, 024304 (2025).
[5] R. Rodríguez-Guzmán, Y. M. Humadi, and L. M. Robledo, Eur. Phys. J. A **56**, 43 (2020).
[6] K. Okada, T. Wada, R. Capote, and N. Carjan, Phys. Rev. C **107**, 034608 (2023).
[7] M. V. Stoitsov, N. Schunck, M. Kortelainen, N. Michel, H. Nam, E. Olsen, J. Sarich, and S. Wild, Comput. Phys. Commun. **184**, 1592 (2013).
[8] J. Bartel, P. Quentin, M. Brack, C. Guet, and H.-B. Håkansson, Nucl. Phys. A **386**, 79 (1982).
[9] E. Chabanat, P. bonche, P. Haensel, J. Meyer, and R. Schaeffer, Nucl. Phys. A **635**, 231 (1998).
[10] M. Kortelainen, J. McDonnell, W. Nazarewicz, P.-G. Reinhard, J. Sarich, N. Schunck, M. V. Stoitsov, and S. M. Wild, Phys. Rev. C **85**, 024304 (2012).
[11] N. Sandulescu, P. Schuck, and X. Viñas, Phys. Rev. C **71**, 054303 (2005).
[12] K. Nomura, D. Vretenar, Z. P. Li, and J. Xiang, Phys. Rev. C **104**, 024323 (2021).
[13] B. Maass, W. Ryssens, K. König, M. Bender, D. P. Burdette, J. Clark, A. Dockery, G. Grams, M. Horst, P. Imgram, K. Minamisono, P. Müller, P. Müller, W. Nörtershäuser, S. V. Pineda, S. Rausch, L. Renth, B. J. Rickey, D. Santiago-Gonzalez, G. Savard, F. Sommer, and A. A. Valverde, Phys. Rev. Lett. **135**, 202501 (2025).
[14] S. Ansari, J.-M. Régis, J. Jolie, N. Saed-Samii, N. Warr, W. Korten, M. Zielińska, M.-D. Salsac, A. Blanc, M. Jentschel, U. Köster, P. Mutti, T. Soldner, G. S. Simpson, F. Drouet, A. Vancraeyenest, G. de France, E. Clémen, O. Stezowski, C. A. Ur *et al.*, Phys. Rev. C **96**, 054323 (2017).
[15] W. Horiuchi, T. Inakura, and S. Michimasa, Phys. Rev. C **105**, 014316 (2022).
[16] M. G. Procter, D. M. Cullen, P. Ruotsalainen, T. Braunroth, A. Dewald, C. Fransen, T. Grahn, P. T. Greenlees, M. Hackstein, K. Hauschild, U. Jakobsson, P. M. Jones, R. Julin, S. Juutinen, S. Ketelhut, A. Lopez-Martens, M. Leino, J. Litzinger, P. J. R. Mason, P. Nieminen *et al.*, Phys. Rev. C **84**, 024314 (2011).
[17] S. Hatakeyama, W. Horiuchi, and A. Kohama, Phys. Rev. C **97**, 054607 (2018).
[18] I. Tanihata, H. Hamagaki, O. Hashimoto, Y. Shida, N. Yoshikawa, K. Sugimoto, O. Yamakawa, T. Kobayashi, and N. Takahashi, Phys. Rev. Lett. **55**, 2676 (1985).

[19] R. J. Glauber, in *Lectures in Theoretical Physics*, edited by W. E. Brittin and L. G. Dunham (Interscience, New York, 1959), Vol. 1, p. 315.
[20] B. Abu-Ibrahim, W. Horiuchi, A. Kohama, and Y. Suzuki, Phys. Rev. C **77**, 034607 (2008); **80**, 029903(E) (2009); **81**, 019901(E) (2010).
[21] W. Horiuchi, T. Inakura, T. Nakatsukasa, and Y. Suzuki, Phys. Rev. C **86**, 024614 (2012).
[22] W. Horiuchi, Y. Suzuki, P. Capel, and D. Baye, Phys. Rev. C **81**, 024606 (2010).
[23] W. Horiuchi, T. Inakura, T. Nakatsukasa, and Y. Suzuki, JPS Conf. Proc. **6**, 030079 (2015).
[24] W. Horiuchi, S. Hatakeyama, S. Ebata, and Y. Suzuki, Phys. Rev. C **93**, 044611 (2016).
[25] T. Nagahisa and W. Horiuchi, Phys. Rev. C **97**, 054614 (2018).
[26] Y. Yano, Nucl. Instrum. Methods Phys. Res. Sect. B **261**, 1009 (2007).
[27] W. Horiuchi, Y. Suzuki, and T. Inakura, Phys. Rev. C **89**, 011601(R) (2014).